# COMPUTATIONAL METHODS FOR RAIL VEHICLE STEADY-STATE CURVING ANALYSIS

**M. L. Nagurka,** Doctoral Candidate
Department of Mechanical Engineering
Massachusetts Institute of Technology
Cambridge, Massachusetts

**C. E. Bell**
Jet Propulsion Laboratory
Pasadena, California

**J. K. Hedrick,** Associate Professor and **D. N. Wormley,** Professor
Department of Mechanical Engineering
Massachusetts Institute of Technology
Cambridge, Massachusetts

ABSTRACT

Computational methods are described to predict wheelset steady-state curving performance. A methodology is developed to compute various performance measures including wheelset lateral excursion, angle of attack, lateral and vertical wheel-rail forces as well as wheel-rail wear indices.

A discussion of the required degrees of freedom, appropriate coordinate systems, and creep force representation of a nonlinear wheelset model is presented. In addition, assumptions required to characterize single-point and two-point wheel-rail contact are described.

Equilibrium conditions for a wheelset result in coupled sets of nonlinear algebraic equations, which are solved using nested iteration loops. Using this numerical solution procedure, typical performance results are presented.

NOMENCLATURE

| | |
|---|---|
| $a$ | half of track gage |
| $a_e$ | longitudinal semi-axis of contact patch ellipse |
| $A_r$ | area of contact |
| $b_e$ | lateral semi-axis of contact patch ellipse |
| $B$ | proportionality constant |
| $d_c$ | critical plastic displacement |
| $f_{ij_N}$ | nominal creep coefficients |
| $f_{11}$ | lateral creep coefficient |
| $f_{12}$ | lateral/spin creep coefficient |
| $f_{22}$ | spin creep coefficient |
| $f_{33}$ | longitudinal creep coefficient |
| $\bar{F}_c$ | creep force vector (with components $F_{CPX}$, $F_{CPY}$, and $M_{CP}$ in longitudinal, lateral, and normal contact patch directions, respectively) |

| | |
|---|---|
| $F_{CPX}, F_{CPY}$ | creep force in longitudinal, lateral contact patch direction |
| $F'_{CPX}, F'_{CPY}$ | unlimited creep force in longitudinal, lateral contact patch direction |
| $F_{CXi}$ | longitudinal track frame component of creep force at i-th contact patch; i = L (left), R(right) for single-point; i = LT (left tread), LF (left flange), R(right) for two-point |
| $F_{CYi}$ | lateral track frame component of creep force at i-th contact patch; i = L (left), R(right) for single-point; i = LT (left tread), LF(left flange), R(right) for two-point |
| $F_{CZi}$ | vertical track frame component of creep force at i-th contact patch; i = L (left), R(right) for single-point; i = LT (left tread), LF (left flange), R(right) for two-point |
| $F_f$ | lateral flange force |
| $F_{lat}$ | wheelset lateral force (in lateral track frame direction) provided by suspension and body (cant deficiency) forces |
| $F_{Ni}$ | normal force at i-th contact patch; i = L (left), R (right) for single-point; i = LT (left tread), LF (left flange), R (right) for two-point |
| $F_{NYi}$ | lateral track frame component of normal force at i-th contact patch; i = L (left), R(right) for a single-point; i = LT (left tread), LF (left flange), R (right) for two-point |
| $F_{NZi}$ | vertical track frame component of normal force at i-th contact patch; i = L (left), R (right) for single-point; i = LT (left tread), LF (left flange), R (right) for two-point |
| $F_{rail_L}, F_{rail_R}$ | lateral rail reaction force at left, right rail |
| $F'_R$ | unlimited resultant creep force |
| $F_t$ | longitudinal thrust or drawbar force (in longitudinal track frame direction) |
| $F_{YL}, F_{YR}$ | net force in lateral track frame direction at left, right wheel (sum of lateral components of creep and normal forces) Note: For lateral equilibrium: $F_{YL} + F_{YR} + F_{lat} = 0$ |
| $F_{YLF}, F_{YLT}$ | net force in lateral track frame direction at flange, tread contact patch of left wheel (sum of lateral components of creep and normal forces) |
| $F_{ZLF}, F_{ZLT}$ | net force in vertical track frame direction at flange, tread contact patch of left wheel (sum of vertical components of creep and normal forces) Note: For two-point contact: $F_{ZLF} + F_{ZLT} - V_L = 0$ |
| $g_i( )$ | function of ( ) |
| $h_l$ | thickness of wear particles |
| $k_r$ | effective lateral rail stiffness |
| $(L/V)_{lower}, (L/V)_{upper}$ | lower, upper bounds on maximum lateral-to-vertical force ratio at flanging wheel (from Nadal's limit) |
| $M_{CP}$ | creep moment normal to contact patch |
| $M_{CYi}$ | lateral track frame component of creep moment at i-th contact patch; i = L (left), R (right) for single-point; i = LT (left tread), LF (left flange), R (right) for two-point |

$M_{CZi}$ vertical track frame component of creep moment at i-th contact patch; i = L (left), R (right) for single-point; i = LT (left tread), LF (left flange), R (right) for two-point

$M_{yaw}$ wheelset yaw moment (in vertical wheelset frame direction) provided by suspension forces

N normal load (same as $F_{Ni}$)

$N_N$ nominal normal load

$P_{in}, P_{out}$ input, output power

R curve radius, often expressed in degree curve, D, where $D = \frac{360}{\pi} \sin^{-1} (\frac{50}{R})$ with R in ft

$r_i$ rolling radius measured from wheelset spin axis to i-th contact patch; i = L (left), R (right) for single-point, i = LT (left tread), LF (left flange), R (right) for two-point

$r_o$ rolling radius for centered wheelset; nominal rolling radius

S sliding distance

$T_d$ wheelset drive/brake torque

V forward speed

$V_L, V_R$ external vertical load acting on left, right wheel (in negative vertical track frame direction) provided by body and suspension forces

$W_V$ wear volume

$W_1$ contact patch work per distance traveled (in force units) $W_1 = \bar{F}_c \cdot \bar{\xi}$

$W_2$ contact patch work per distance traveled ($W_1$) divided by contact patch area

$x_T, x_W$ longitudinal displacement in track, wheelset frame

$y_{fc}$ flange clearance

$y_{rail_L}, y_{rail_R}$ lateral displacement of left, right rail

$y_T, y_W$ lateral displacement in track, wheelset frame

$z_T, z_W$ vertical displacement in track, wheelset frame

$\dot{\beta}$ spin perturbation rate (from pure rolling angular speed)

$\delta_i$ contact angle at i-th contact patch; i = L (left), R (right) for single-point; i = LT (left tread), LF (left flange), R (right) for two-point

$\Delta x_i$ longitudinal displacement of i-th contact patch from vertically below wheelset axis

$\Delta_z$ vertical distance between points of flange and tread contact

$\varepsilon$ creep force saturation constant

$\mu$ coefficient of friction

$\mu_f$ coefficient of flange friction

$\bar{\xi}$ creepage vector (with components $\xi_{xi}$, $\xi_{yi}$, and $\xi_{spi}$ in longitudinal, lateral, and normal contact patch directions, respectively)

$\xi_R$ resultant creepage

$\xi_{spi}$ spin creepage in normal contact patch direction at i-th contact patch

$\xi_{xi}$ longitudinal creepage at i-th contact patch

$\xi_{yi}$ lateral creepage at i-th contact patch

$\rho$ wheelset spin speed per forward speed (or, wheelset pitch per distance traveled)

$$\rho = \frac{\Omega}{V} = \frac{1}{r_o} + \frac{\dot{\beta}}{V}$$

$\phi_d$ cant deficiency (lateral unbalance load)

$$\phi_d = \frac{V^2}{Rg} - \phi_{SE}$$

$\phi_{SE}$ track superelevation (or bank) angle

$\phi_w$ wheelset roll angle with respect to track plane

$\psi_w$ wheelset angle of attack, or yaw angle with respect to radial alignment

$\Omega$ wheelset spin speed

INTRODUCTION

Rail vehicle steady-state curving analysis provides an evaluation of the effects of vehicle design parameters, curvature, and cant deficiency (lateral unbalance) on wheel-rail forces and geometry. Studies have indicated the value of minimizing wheel-rail forces and wheelset angles of attack since large forces and radial misalignment lead to increased wheel-rail wear resulting in wheel and track deterioration (and noise), enhance the potential danger of derailment due to wheel climb, and raise fuel consumption because of increased rolling resistance in curves.

Analytic models of rail vehicle curve negotiation were reported over fifty years ago (1,2). These early works assumed rigid frame vehicles negotiating constant radius curves. They lacked an appropriate treatment of the frictional behavior that arises between a rail and wheel which is rolling with slip, known as creep. It took thirty years before any significant theoretical progress was made in developing the relationships between the creep mechanisms and the associated wheel-rail shear forces (by Vermeulen and Johnson (3) and Kalker (4)). Kalker provided comprehensive mathematical models of the wheel-rail interaction when slip is present assuming elastic deformation and elliptical contact zones.

Newland (5) and Boocock (6) each described simple linear models to study steady-state curving. Conical wheels, flexible primary suspensions, and wheel-rail interaction effects due to creep and wheel-rail geometry were assumed. By linearizing the analysis, each developed efficient computational tools which were used to predict slip and flange contact boundaries that define regions of "acceptable" curving performance as functions of cant deficiency and track curvature. However, because of the imposed linearization, the results are applicable only to steady curving conditions involving large radius curves.

Bell, Horak, and Hedrick (7,8) exercised simple linear models to gain a fundamental understanding of steady-state curving and stability mechanics of rail vehicles running with conventional and radial trucks. They demonstrated that the self-steering truck allows improved wheelset alignment in curves without a sacrifice in dynamic performance on tangent track.

Nonlinear steady-state curving models were developed by Elkins and Gostling (9). They incorporated large wheel-rail contact angles and Kalker's nonlinear creep theory while retaining linear suspension elements. Law and Cooperrider (10) and Hedrick, et al. (11) explored the effects of nonlinear suspension components. In doctoral research, Bell (12) developed a detailed nonlinear steady-state curving model to study the effects of nonlinear suspension and wheel-rail profile on conventional, self-steering radial, and forced-steering trucks. Using this model, Bell and Hedrick (13) showed that the curve negotiation capability of forced-steered trucks is significantly improved over conventional and self-steering radial trucks.

The majority of previous steady-state curving studies have assumed that each wheel of the vehicle contacts the rails at a single point. For some wheel-rail

profiles this is a simplistic view of the flange contact mechanism. The vehicle curving performance studies of Marcotte, et al. (14) accounted for the possibility of two-point wheel-rail contact by using a wheel profile composed of a tread and flange segment each of constant (but different) conicity.

The basic element of the rail vehicle steering and support system is the wheelset. The contact and friction mechanisms which develop at the wheel-rail interfaces have a dominant effect on vehicle curving behavior. The curving performance of a vehicle is a direct function of the ability of its wheelsets to negotiate a curve.

This paper addresses the computational methods required to characterize rail vehicle steady-state curving behavior by focusing on wheelset mechanics. A number of performance indices, designed to measure the ability of a vehicle or wheelset to negotiate a curve, are introduced. A detailed model of the nonlinear forces which act at the wheel due to contact at the rail is developed. The model accounts for nonlinearities due to profile geometry and creep force saturation, and represents single-point and two-point wheel-rail contact at the flanging wheel. Steady-state curving conditions are achieved when the wheelset satisfies force and moment static equilibrium. The equilibrium equations are developed, and appropriate numerical solution procedures involving nested iteration loops are described. In addition, a simple method to accommodate rail flexibility is introduced.

## PERFORMANCE INDICES

Several performance indices have been developed to represent the ability of a rail vehicle to negotiate a curve. A number of simultaneous objectives can be identified, such as perfect steering, prevention of derailment, minimum wheel-rail forces, and minimum wheel-rail wear.

Optimal curve negotiation, or perfect steering, is achieved if each wheelset in a vehicle adopts a radial position and displaces laterally so that it rolls without slip around the curve. As such, the wheelset lateral excursion from the track centerline, $y_w$, and the wheelset angle of attack or yaw angle with respect to radial alignment, $\psi_w$, are natural performance indices. Displacements $y_w$ and $\psi_w$ are defined in Figure 1. An undesirable situation exists when these indices reach large magnitudes. With significant wheelset lateral displacement and radial misalignment, flange contact occurs.

The derailing tendencies of a vehicle are associated with the ratio of lateral flange force to vertical wheel load. When this ratio exceeds a critical value, there exists a situation conducive to a flange-climbing type derailment (15,16).

Several wear indices have been proposed to predict wear rates at the wheel-rail interface. Due to the complex nature of modeling wear, these indices are designed to relate to wear in a relative manner and are used for performance comparisons, rather than to represent actual wear. A list of proposed wear indices appears in Table I. The wheelset angle of attack, $\psi_w$, the creepages (or normalized rates of slippage), $\xi_i$, and the lateral flange force (for a flanging wheel), $F_f$, are related to the wear rate (5,6). The effect of increased $\psi_w$, $\xi_i$, and/or $F_f$ is to increase wear at the wheel-rail contact point.

No comprehensive verification of the proposed wear indices has been conducted. Limited tests by British Rail and I.I.T. have shown potentially useful trends (19,21). Dry wear laboratory tests by British Rail (22) have suggested that the wear rate can be expressed in terms of creep force, creepage, and Hertzian contact area. Wide-scale experimental validation of wear models needs to be undertaken to identify which indices can be related directly with wear.

In this paper the forces and creepages at the wheel-rail interface are computed so that most of the indices listed in Table I can be predicted.

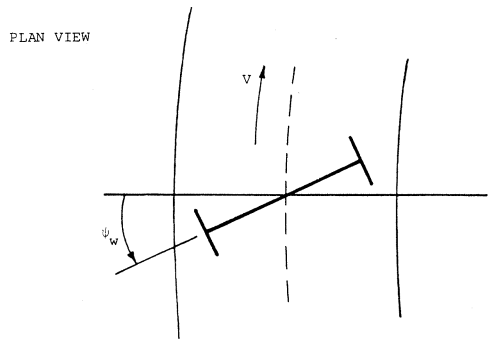


a) Angle of Attack

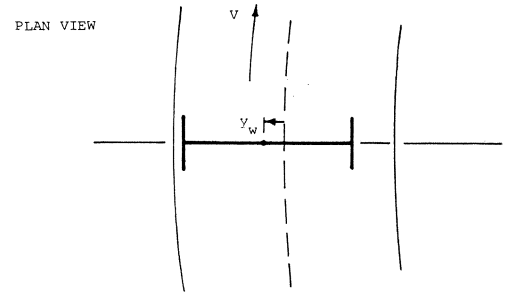


b) Lateral Wheelset Excursion

Fig. 1 Definition of angle of attack and lateral wheelset excursion

Table I Proposed Wear Indices*

| WEAR INDEX | | SOURCE |
|---|---|---|
| $\psi_w$ | Angle of Attack | (5,6) |
| $\xi_i$ | Creepage | |
| $F_f$ | Flange Force | |
| $F_f \psi_w$ | Flange Wear Index | (14) |
| $\mu_f F_f \sqrt{(\Delta_z/r_{LT})^2+(\psi_w \tan\delta_{LF})^2}$ | Two-Point Flange Wear Index | (14) |
| $V_i \xi_R$ | Tread Wear Index | (17) |
| $W_1=\bar{F}_c \cdot \bar{\xi}$ | Contact Patch Work | (18) |
| $W_2 = \frac{W_1}{\pi a_e b_e}$ | Contact Patch Work/Area | (19) |
| $W_v = \frac{B\, h_1 A_r S}{d_c}$ | Wear Volume | (20) |

*Variables in Table I are defined in the nomenclature.

GEOMETRIC CONSTRAINTS

A. Coordinate Systems

A free wheelset negotiating a constant radius curve is exposed to track curvature and lateral force unbalance inputs. The track curvature is given by 1/R, where R is the curve radius assumed constant. The lateral force unbalance is usually expressed in terms of cant deficiency, $\phi_d$, defined as the angle between (1) the resultant of the "centrifugal force", $mV^2/R$, and the weight, mg, and (2) the normal into the rail plane. When $\phi_d=0$, a condition of "balanced running" is achieved for which the components of centrifugal force and weight parallel to the rail plane cancel each other. For comfort and safety the maximum cant deficiency loads are limited to low levels in the U.S. (about 6° of inboard unbalance and 3° of outboard unbalance (12)). Track curvature is therefore considered the dominant curving input.

Assuming continuous wheel-rail contact, a wheelset negotiating a constant radius track at constant speed has two independent degrees of freedom: lateral and yaw displacements, $y_w$ and $\psi_w$, respectively. The convention for positive $y_w$ and $\psi_w$ displacements is shown in Figure 1. In this paper, right-handed curves are considered, and thus positive $y_w$ is associated with displacements toward the left rail. Track and wheelset coordinate systems are introduced in Figure 2. Contact angles ($\delta_L$,$\delta_R$), rolling radii ($r_L$,$r_R$), and wheelset roll angle relative to the track plane ($\phi_w$) are defined in Figure 3.

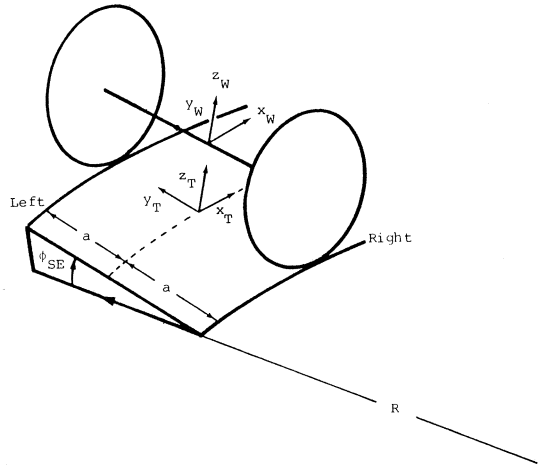


Fig. 2 Track and wheelset coordinate systems

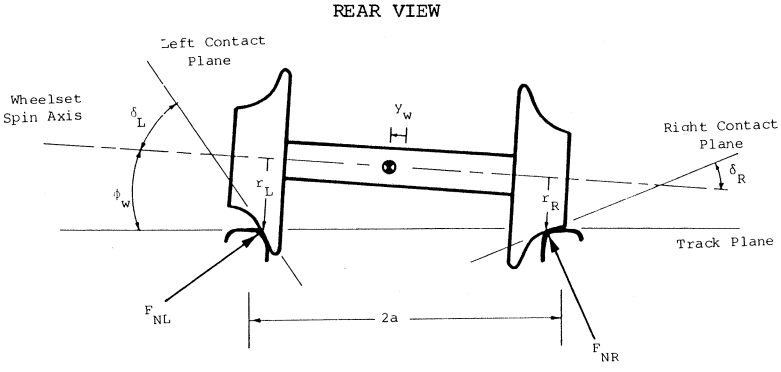


Fig. 3 Wheel-rail geometry and normal forces assuming single-point contact

B. Wheel-Rail Profile Geometry

For a wheelset which never loses contact with the rails, the rolling radii, contact angles, and wheelset roll angle are functions of the net wheelset-rail lateral excursion for a given wheel-rail profile. These functions (rolling radii and contact angles) are shown in Figure 4 for a typical new wheel on worn rail profile on standard gage (23). For this profile, the flange clearance is $y_{fc}$ = 0.32 in. When the wheelset lateral excursion minus the rail lateral excursion is less than flange clearance, tread contact occurs. Flanging at the left wheel occurs when the wheelset lateral excursion with respect to the left rail equals or exceeds flange clearance. Note that for severe flanging the contact angle approaches 65°.

The rolling radii, contact angles, and roll angle are wheel-rail geometric constraint variables since they are functions of the net wheelset-rail lateral displacement. These variables indicate the nature of wheel-rail contact as the wheelset is displaced laterally. If the rolling radii and contact angles are single-valued functions of the lateral excursion, single-point contact occurs at both wheels for all displacements. This represents a continuous single-point contact approximation, shown in Figure 4 with solid lines. As the wheelset is laterally displaced, the left wheel shifts from tread to flange contact, while the inner wheel maintains tread contact. For other profiles (the dashed lines in Figure 4) the left rolling radius and left contact angle have steep slopes at net lateral excursions equal to flange clearance. This indicates the possibility that multiple wheel-rail contact points exist at the flanging (left) wheel. As before, single-point tread contact occurs for net lateral excursions less than flange clearance, corresponding to the situation drawn in Figure 5a. For net lateral excursions equal to flange clearance, it is assumed that two-point contact occurs at the flanging wheel. This is depicted in Figure 5b, where the rail head is shown to contact simultaneously both the tread and flange of the flanging (outer) wheel. The inner wheel maintains single-point tread contact. For net lateral excursions larger than flange clearance, a situation conducive to derailment exists since single-point flange contact occurs at the flanging wheel (Figure 5c).

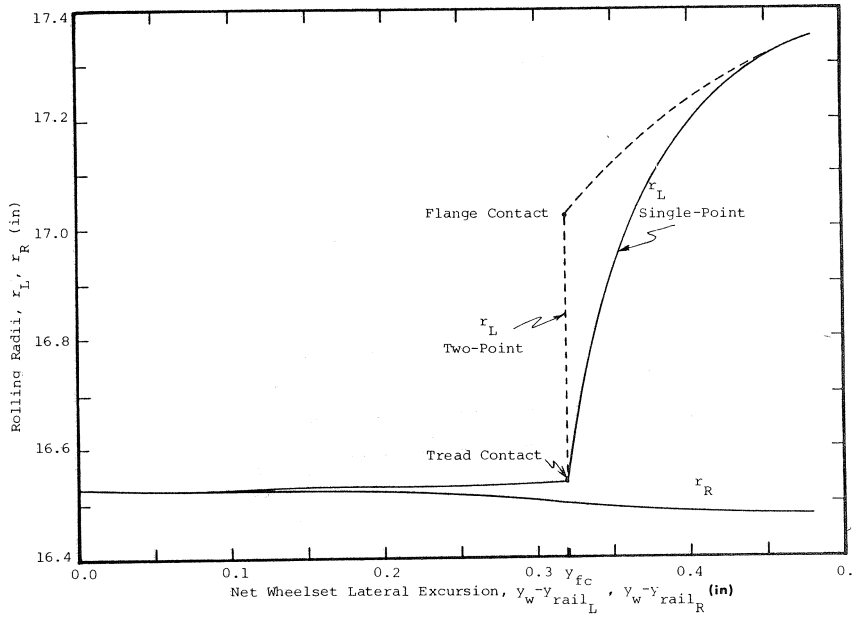


Fig. 4a: Rolling radii vs net wheelset lateral excursion for new wheel on worn rail

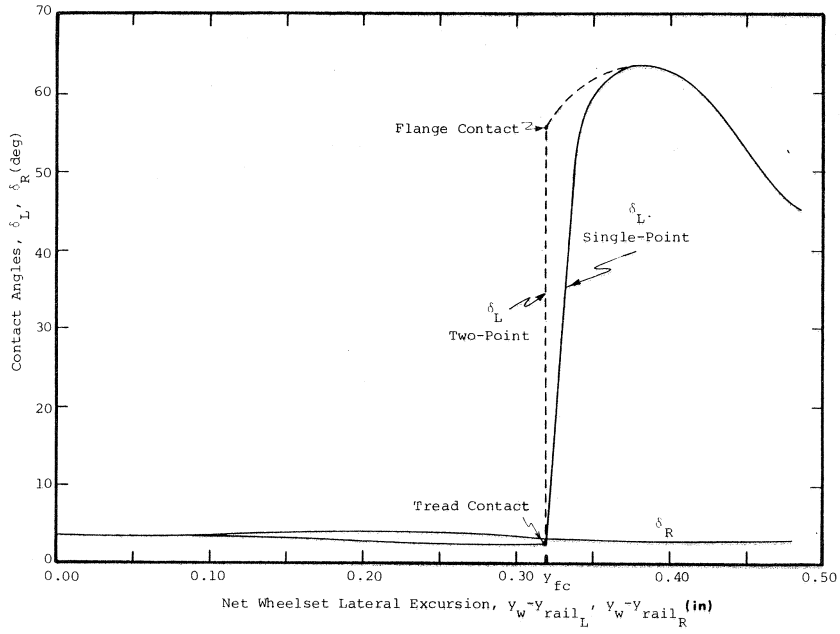


Fig. 4b Contact angles vs. net wheelset lateral excursion for new wheel on worn rail

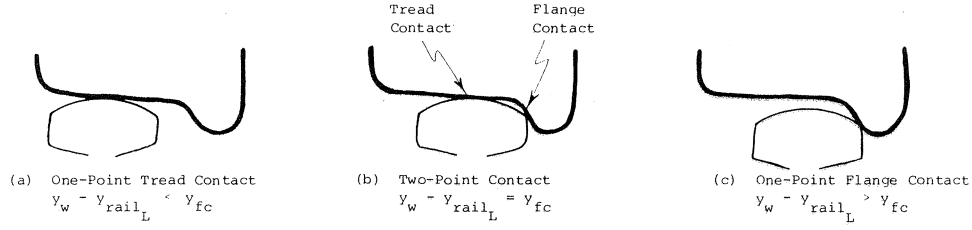


Fig. 5 Left wheel-rail contact

Some profiles are designed to achieve single-point wheel-rail contact for all realistic values of lateral displacement. Many new wheel profiles, such as the AAR 1 in 20, contact the rails at multiple points during normal use. Naturally, wheel (and rail) profiles change with time due to wear during service life.

## WHEELSET EQUILIBRIUM CONDITIONS

For a wheelset negotiating a curve, a difference occurs between the actual velocity and the velocity in pure rolling of the contact points resulting in partial slip or creepage of the wheels relative to the rails. Normal loads acting on a slipping wheelset result in the generation of creep forces. Due to the action of creep, the lateral and yaw degrees of freedom of a wheelset are coupled.

Each point of wheel-rail contact is a patch of finite area, where a state

between pure-roll and pure-slip exists. During the last ten years there has been a significant improvement in the understanding of this friction mechanism and in computational programs to predict it. Kalker (4) developed linear, simplified nonlinear, and exact nonlinear theories and programs. In this paper a "heuristic" (3) creep force model* is used which is computationally fast and reasonably accurate. The creep forces and moment at each contact patch can be resolved into longitudinal, lateral, and vertical components in the track frame.

Whereas creep forces act in the plane of each contact patch, normal forces act perpendicular to the plane. These forces can be resolved into lateral and vertical components in the track frame. For single-point wheel-rail contact at the left and right wheels, the resolved normal force components from Figure 3 are

$$\begin{aligned} F_{NYL} &= -F_{NL}\sin(\delta_L + \phi_w) \\ F_{NZL} &= F_{NL}\cos(\delta_L + \phi_w) \\ F_{NYR} &= F_{NR}\sin(\delta_R - \phi_w) \\ F_{NZR} &= F_{NR}\cos(\delta_R - \phi_w) \end{aligned} \tag{1}$$

The sum of the lateral components of the normal force is sometimes referred to as the "gravitational stiffness force".

The static equilibrium conditions for a wheelset negotiating a constant radius curve can be expressed by eight algebraic equations, six for the wheelset and one for each rail. The rail is assumed to only have a lateral degree of freedom (Figure 6), i.e., overturning motion has been neglected. The equilibrium equations are

Wheelset:

$$\Sigma F_{x_T} = 0 \tag{2}$$

$$\Sigma F_{y_T} = 0 \tag{3}$$

$$\Sigma F_{z_T} = 0 \tag{4}$$

$$\Sigma M_{x_w} = 0 \tag{5}$$

$$\Sigma M_{y_w} = 0 \tag{6}$$

$$\Sigma M_{z_w} = 0 \tag{7}$$

Left Rail:

$$\Sigma F_{y_T} = 0 \tag{8}$$

Right Rail:

$$\Sigma F_{y_T} = 0 \tag{9}$$

where external and inertial forces/moments are summed on the left. Equations (2)-(4) are wheelset force equilibrium equations, (5)-(7) are wheelset moment equations and (8)-(9) are the left and right rail lateral force equations.

In steady-state curving the rails can be modeled approximately as linear springs as shown in Figure 6. Each rail displaces laterally a distance related to the net lateral wheel force, i.e.,

$$y_{rail_L} = \frac{F_{YL}}{k_r} \tag{10}$$

$$y_{rail_R} = \frac{F_{YR}}{k_r} \tag{11}$$

*See Appendix A.

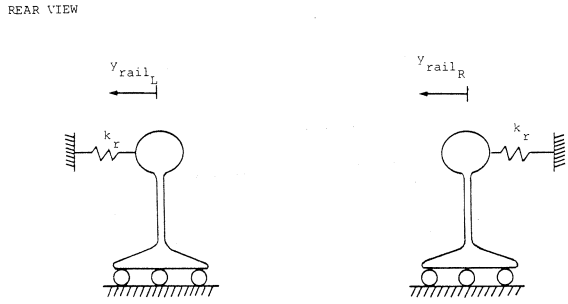


Fig. 6 Flexible rail model

where $F_{YL}$ and $F_{YR}$ are the net lateral wheel forces and are composed of creep and normal forces. The typical range of effective lateral rail stiffness values (24) is 25,000 lb/in to 80,000 lb/in.

Two nonlinear models have been developed to predict the steady-state curving behavior of a single wheelset. Both models assume that the wheelset is in force and moment static equilibrium. The difference between the models is that one assumes that single-point wheel-rail contact occurs at both wheels of the wheelset; the other model assumes that two-point tread-flange contact occurs at the outer wheel and single-point tread contact occurs at the inner wheel of the wheelset. The following two sections formulate the equilibrium conditions for these two models.

A. Single-Point Contact

A free-body diagram of a wheelset with single-point contact at each wheel-rail interface is shown in Figure 7a. All forces and moments are resolved in track coordinates, except for the wheelset drive/brake torque, $T_d$, which acts about the spin axis. This drive/brake torque can be considered to be a specified input. Other inputs are: (1) the vertical loads on the left and right wheels, $V_L$ and $V_R$, respectively, acting in the negative $z_T$ direction, (2) the thrust or drawbar force, $F_t$, acting at the wheelset center of mass in the $x_T$ direction, (3) the wheelset lateral force, $F_{lat}$, acting in the track plane in the $y_T$ direction, and (4) the wheelset yaw moment, $M_{yaw}$, acting about the $z_W$ axis. Figure 7b shows a rear view of the wheel and rail force equilibrium.

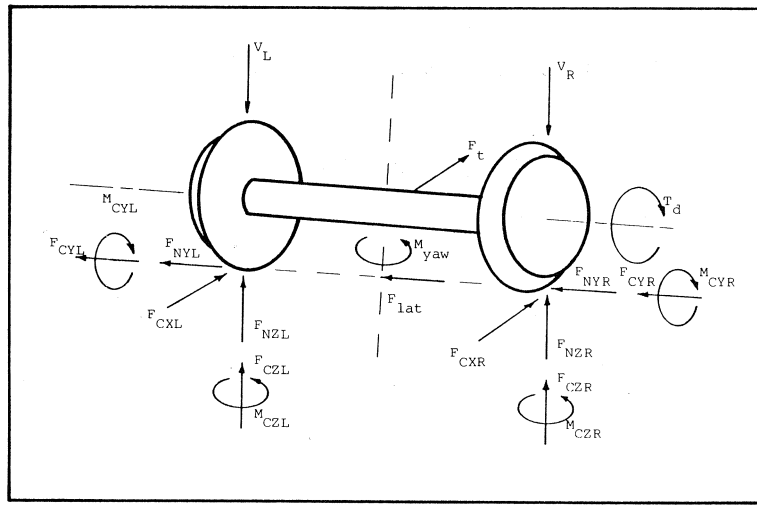


Fig. 7a Wheelset free-body diagram: single-point wheel-rail contact

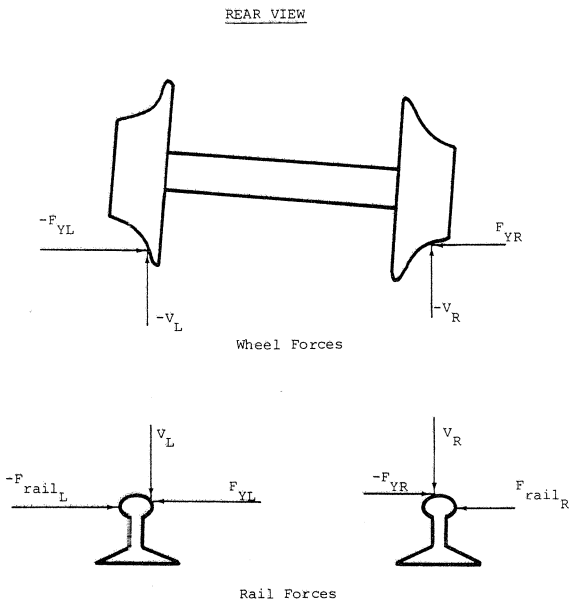


Fig. 7b Wheel and rail forces for single-point contact

Assuming single-point contact at the left and right wheel-rail interfaces and small roll and yaw angles, the following steady-state equilibrium conditions apply:

WHEELSET

LONGITUDINAL

$$\Sigma F_{x_T} = 0 = F_{CXL} + F_{CXR} + F_t \tag{12}$$

LATERAL

$$\Sigma F_{y_T} = 0 = F_{NYL} + F_{CYL} + F_{NYR} + F_{CYR} + F_{lat} \tag{13}$$

VERTICAL

$$\Sigma F_{z_T} = 0 = F_{NZL} + F_{CZL} + F_{NZR} + F_{CZR} - V_L - V_R \tag{14}$$

ROLL

$$\Sigma M_{x_w} = 0 = (F_{NZL} + F_{CZL} - F_{NZR} - F_{CZR})a + (V_R - V_L)a \tag{15}$$

SPIN

$$\begin{aligned}\Sigma M_{y_w} = 0 = {} & -r_L[F_{CXL} + \psi_w\{F_{CYL} + F_{NYL} - (F_{CZL} + F_{NZL})\tan\delta_L\}] \\ & -r_R[F_{CXR} + \psi_w\{F_{CYR} + F_{NYR} - (F_{CZR} + F_{NZR})\tan\delta_R\}] \\ & +M_{CYL} + M_{CYR} + \phi_w(M_{CZL} + M_{CZR}) + T_d\end{aligned} \tag{16}$$

YAW

$$\Sigma M_{z_w} = 0 = -(F_{CXL} - F_{CXR})a - \psi_w\{(F_{NYL} + F_{CYL})(a - r_L\tan\delta_L) - (F_{NYR} + F_{CYR})(a - r_R\tan\delta_R)\} + M_{CZL} + M_{CZR} + \phi_w(M_{CYL} + M_{CYR}) + M_{yaw} \quad (17)$$

RAIL

LATERAL LEFT

$$\Sigma F_{y_T} = 0 = F_{NYL} + F_{CYL} + F_{rail_L} \quad (18)$$

LATERAL RIGHT

$$\Sigma F_{y_T} = 0 = F_{NYR} + F_{CYR} + F_{rail_R} \quad (19)$$

Here the lateral rail reaction forces, $F_{rail_L}$ and $F_{rail_R}$, are functions of $y_w - y_{rail_L}$ and $y_w - y_{rail_R}$, respectively.

Equations (12) - (19) represent eight coupled nonlinear algebraic equations. Assuming $V_L$, $V_R$, $F_{lat}$, and $M_{yaw}$ are known, the equations can be solved for the following eight independent variables: $F_t$, $y_w$, $F_{NZL}$, $N_{NZR}$, $\Omega$, $\psi_w$, $y_{rail_L}$, $y_{rail_R}$. These variables can be used to calculate all wheel-rail forces. The contact angle and roll angle are specified since $y_w - y_{rail_L}$ and $y_w - y_{rail_R}$ are known, and thus the resultant normal forces and the lateral components of the normal forces can be calculated from $F_{NZL}$ and $F_{NZR}$. The creep forces at the left and right contact patches can be computed since the creepages (which are functions of $y_w - y_{rail_L}$, $y_w - y_{rail_R}$, $\Omega$, and $\psi_w$) and the normal forces are known. Equations (12) - (19) can alternatively be solved for the following variables if $V_L$, $V_R$, $y_w$, and $\psi_w$ are specified: $F_t$, $F_{lat}$, $F_{NZL}$, $F_{NZR}$, $\Omega$, $M_{yaw}$, $y_{rail_L}$, $y_{rail_R}$. Later in this article, the numerical technique required to solve for this latter set of unknowns is described. Finally, for the case of rigid rails, $y_{rail_L} = y_{rail_R} = 0$ and the wheelset equilibrium equations, equations (12) - (17), decouple from the lateral rail force equations, equations (18) and (19), leaving a system of six equations with six unknowns.

The thrust in the longitudinal track direction defines the drawbar force, $F_t$, which must be applied to the wheelset for it to traverse the curve in steady-state. The lateral force, $F_{lat}$, is provided by suspension and body (cant deficiency) forces. It equilibrates the lateral components of creep and normal forces to yield static equilibrium in the lateral direction. Suspension forces also give rise to the yaw moment, $M_{yaw}$, which balances the moments in the yaw direction due to creep and normal forces. The vertical loads which act on the left and right wheels, $V_L$ and $V_R$, respectively, are provided by suspension and body forces. The sum and difference of the vertical and roll equations yield the following equations for the vertical loads:

$$V_L = F_{NZL} + F_{CZL} \quad (20)$$

$$V_R = F_{NZR} + F_{CZR} \quad (21)$$

The rotational velocity of the wheelset is determined by the spin equation, which balances the moments about the wheelset spin (bearing) axis. The wheelset drive/brake torque, $T_d$, is balanced principally by longitudinal creep forces.

B. Two-Point Contact

The wheelset model appropriate for two-point contact analysis assumes simultaneous tread and flange contact at the outer (flanging) wheel and single-point contact at the inner wheel. The lateral displacement of the wheelset with

respect to the left rail is fixed at flange clearance and thus the contact geometry of the tread and flange contact points at the left wheel is fixed even though the forces may vary. Figure 8 shows the free-body wheel and rail forces for two-point contact. The steady-state force and moment equilibrium equations for the case of two-point contact are similar to equations (12)-(19) with new terms to account for the additional contact point. The two-point contact formulation is statically-determinate due to the facts that (1) the net lateral excursion at the left wheel is constrained to equal the flange clearance, and (2) the normal forces have components in the lateral as well as vertical directions. This implies that the contact geometry at the tread and flange contact points of the flanging wheel is known and that the normal force at the flange contact point can be determined from the lateral force balance equation. The complete equations are shown below:

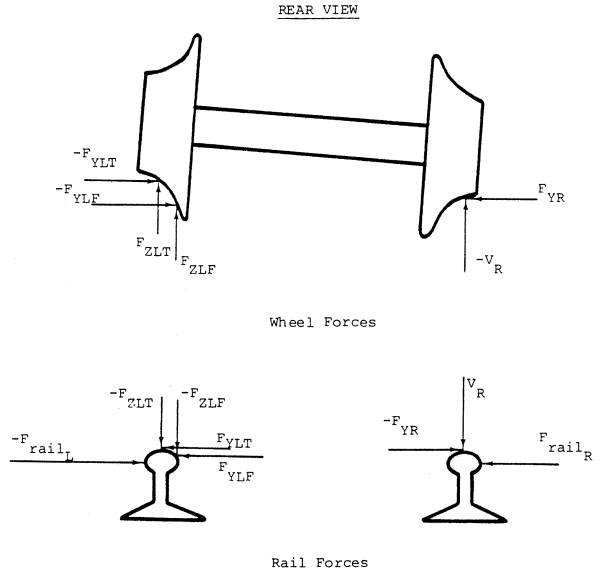


Fig. 8 Wheel and rail forces for two-point contact

WHEELSET

LONGITUDINAL

$$\Sigma F_{x_T} = 0 = F_{CXLT} + F_{CXLF} + F_{CXR} + F_t \quad (22)$$

LATERAL

$$F_{y_T} = 0 = F_{NYLT} + F_{CYLT} + F_{NYLF} + F_{CYLF} + F_{NYR} + F_{CYR} + F_{lat} \quad (23)$$

VERTICAL

$$\Sigma F_{z_T} = 0 = F_{NZLT} + F_{CZLT} + F_{NZLF} + F_{CZLF} + F_{NZR} + F_{CZR} - V_L - V_R \quad (24)$$

ROLL

$$\Sigma M_{x_w} = 0 = (F_{NZLT} + F_{CZLT} + F_{NZLF} + F_{CZLF} - F_{NZR} - F_{CZR})a - (V_R - V_L)a \quad (25)$$

SPIN

$$\Sigma M_{y_w} = 0 = -r_{LT}[F_{CXLT} + \psi_w\{F_{CYLT} + F_{NYLT} - (F_{CZLT} + F_{NZLT})\tan\delta_{LT}\}] - r_{LF}[F_{CXLF} + \psi_w\{F_{CYLF} + F_{NYLF} - (F_{CZLF} + F_{NZLF})\tan\delta_{LF}\}] - r_R[F_{CXR} + \psi_w\{F_{CYR} + F_{NYR} - (F_{CZR} + F_{NZR})\tan\delta_R\}] + M_{CYLT} + M_{CYLF} + M_{CYR} + \phi_w(M_{CZLT} + M_{CZLF} + M_{CZR}) + T_d \quad (26)$$

YAW

$$\Sigma M_{z_w} = 0 = -(F_{CXLT} + F_{CXLF} - F_{CXR})a - \psi_w\{(F_{NYLT} + F_{CYLT})(a - r_{LT}\tan\delta_{LT}) + (F_{NYLF} + F_{CYLF})(a - r_{LF}\tan_{LF}) - (F_{NYR} + F_{CYR})(a - r_R\tan\delta_R)\} + M_{CZLT} + M_{CZLF} + M_{CZR} + \phi_w(M_{CYLT} + M_{CYLF} + M_{CYR}) + M_{yaw} \quad (27)$$

RAIL

LATERAL LEFT

$$\Sigma F_{y_T} = 0 = F_{NYLT} + F_{CYLT} + F_{NYLF} + F_{CYLF} + F_{rail_L} \quad (28)$$

LATERAL RIGHT

$$\Sigma F_{y_T} = 0 = F_{NYR} + F_{CYR} + F_{rail_R} \quad (29)$$

Equations (22) - (29) represent eight coupled nonlinear algebraic equations. In this case the relative wheelset excursion ($y_w - y_{rail_L}$) is fixed at the flange clearance value ($y_{fc}$). Assuming $V_L$, $V_R$, $F_{lat}$, and $M_{yaw}$ are known, the equations can be solved for: $F_t$, $y_w$, $F_{NZLT}$, $F_{NZLF}$, $F_{NZR}$, $\Omega$, $\psi_w$, $y_{rail_R}$. Alternatively, if $V_L$, $V_R$, $y_w$ and $\psi_w$ are specified, the equations can be solved for: $F_t$, $F_{lat}$, $F_{NZLT}$, $F_{NZLF}$, $F_{NZR}$, $\Omega$, $M_{yaw}$, $y_{rail_R}$. For the case of rigid rails the wheelset equations decouple from the rail force equations. The wheelset lateral excursion, $y_w$, equals the flange clearance, $y_{fc}$. If $V_L$, $V_R$, $F_{lat}$, and $\psi_w$ are known, the following variables can be determined from equations (22)-(27): $F_t$, $F_{NZLT}$, $F_{NZLF}$, $F_{NZR}$, $\Omega$, $M_{yaw}$.

The two-point contact model is used to determine the distribution of wheel-rail forces acting at the tread and flange contact points at the flanging wheel. For a wheelset negotiating a shallow curve corresponding to "mild" flanging, the forces at the tread contact point dominate. With tighter curves more severe flanging develops, and the wheel-rail forces gradually grow at the flange contact

point and decrease at the tread contact point. This tradeoff in forces from tread to flange continues with degree curve until all forces act at the flange contact patch. This would occur for a wheelset negotiating an extremely tight curve, and would indicate the danger of derailment as the outer wheel rides high up against the flange. The single-point contact model is appropriate once contact occurs at only the flange contact patch.

A useful relationship between the work index, $W_1$, defined in Table I, and the external forces and moments on the wheelset can be derived by manipulating the equilibrium equations or by writing a power balance equation, i.e.,

$$P_{in} = P_{out} \tag{30}$$

$$P_{in} = V \cdot [F_t - \frac{M_{yaw}}{R} + \rho T_d] \tag{31}$$

$$P_{out} = -VW_1 = -V \sum_{L,R} [F_{CPX_i} \xi_{x_i} + F_{CPY_i} \xi_{y_i} + M_{CP_i} \xi_{sp_i}] \tag{32}$$

Noting from equations (12) and (22) that $F_t = - \sum_{L,R} F_{CXi}$, equation (30) yields:

$$W_1 = \sum_{L,R} F_{CXi} + \frac{M_{yaw}}{R} - \rho T_d \tag{33}$$

Equation (33) is a useful check to ensure that a correct numerical solution of the equilibrium equations has been obtained.

In the full vehicle formulation the wheelset yaw moment is not an external moment and thus equation (33) reduces to that obtained in reference (18), i.e.,

$$W_1 = \sum_{L,R} F_{CXi} - \rho T_d \tag{34}$$

NUMERICAL METHODS

The numerical solution procedures used to solve the coupled equilibrium equations of the single-point contact and two-point contact wheelset models are discussed in the following sections. The procedures assume that the wheelset lateral excursion and angle of attack, as well as the vertical loads acting on the left and right wheels are known. By solving the single-point equations, equilibrium values of lateral force and yaw moment are determined as functions of lateral excursion and angle of attack. For lateral excursions less than and larger than flange clearance this model is appropriate. For some profiles, this model is still appropriate at flange clearance, as was discussed above. For profiles with steep rolling radius-displacement and contact angle-displacement functions at flange clearance, the two-point contact model is applicable since it represents the fact that separate tread and flange contact points actually exist. Solution of the two-point equations gives the equilibrium yaw moment as a function of lateral force and angle of attack.

A. Single-Point Contact

For the case of rigid rails, the wheelset equilibrium conditions are specified by equations (12) through (17), and represent nonlinear algebraic equations coupled due to the fact that the normal and creep forces depend upon each other. First, equations (16), (20), and (21) are solved simultaneously for the wheel-rail contact forces and moments. Then, equations (12), (13), and (17) are used to define the drawbar force, the lateral force, and the yaw moment, respectively, needed to maintain the wheelset in equilibrium.

Two nested iteration loops are used to solve simultaneously the spin, vertical, and roll equations. The inner loop balances the torque about the

wheelset rolling axis by adjusting the spin perturbation rate*, $\dot{\beta}$, to satisfy the spin equation. The outer loop adjusts the vertical component of creep force at each wheel to satisfy the sum and difference of the vertical and roll equations. This procedure is continued until vertical force convergence is achieved, as outlined in the flowchart in Figure 9 and gives the equilibrium values of all contact forces and moments. The longitudinal, lateral, and yaw equations are then applied to solve for the equilibrium values of $F_t$, $F_{lat}$, and $M_{yaw}$, respectively.

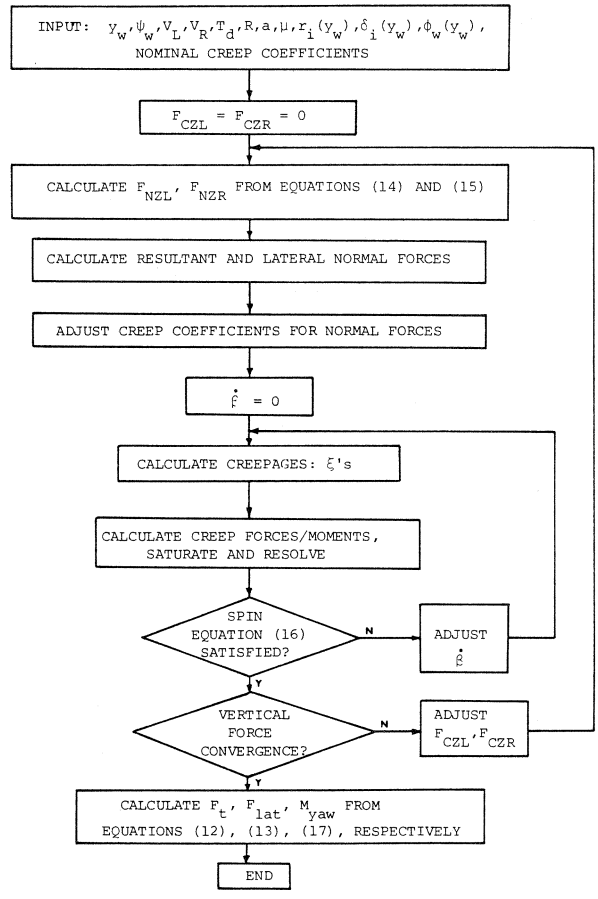


Fig. 9 Flowchart for wheelset equilibrium with rigid rails: single-point contact model

A similar routine to solve the coupled wheelset equilibrium equations was developed by Sweet and Sivak (15) in which the two nested iteration loops are reversed. It should be noted that the creep forces are quite sensitive to small changes in the spin perturbation rate, $\dot{\beta}$.

The nonlinear wheelset routine has been used to predict equilibrium values of wheelset lateral force and yaw moment as functions of wheelset lateral excursion and angle of attack. The vertical loads acting on the left and right wheels are assumed to be known constants, and the rails are modeled as rigid. Mathematically, the functions generated are:

---

* $\Omega \triangleq \frac{V}{r_o} + \dot{\beta}$, where $\dot{\beta}$ is the perturbation from the pure rolling spin velocity.

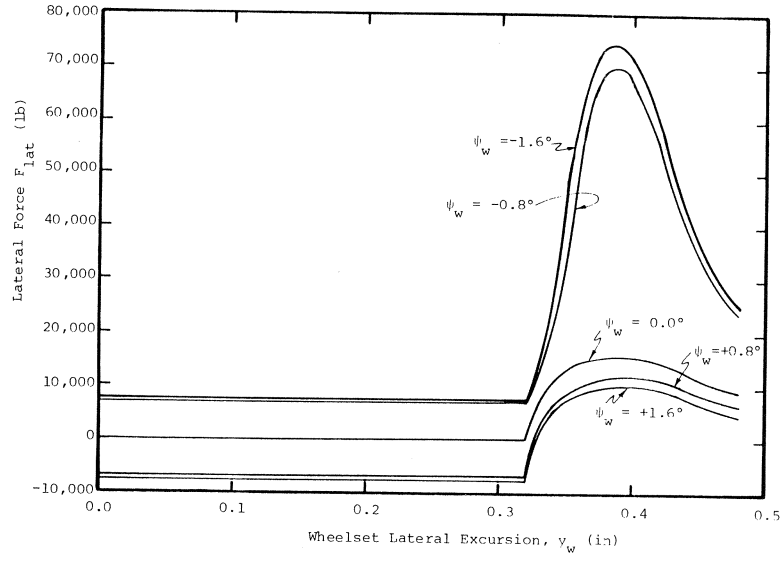


Fig. 10 Lateral Force ($F_{lat}$) vs. lateral excursion ($y_w$) (axle load = 25,000 lb; $\mu$ = 0.3; rigid rails)

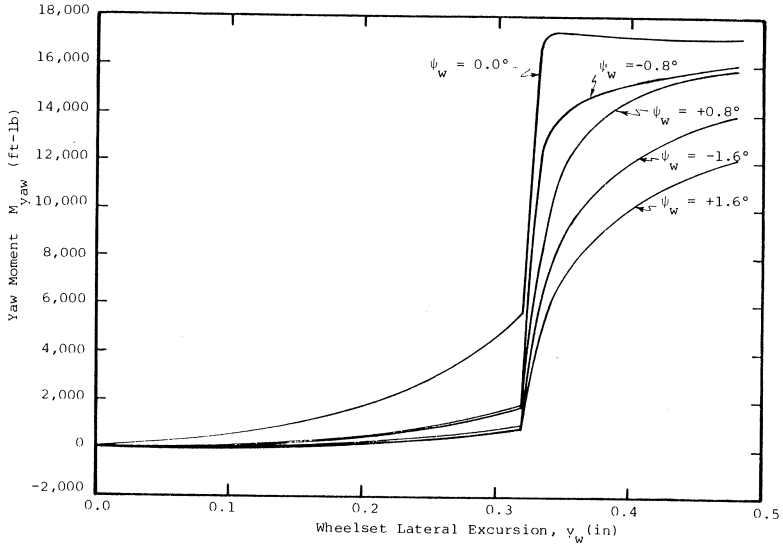


Fig. 11 Yaw moment ($M_{yaw}$) vs. lateral excursion ($y_w$) (axle load = 25,000 lb; $\mu$ = 0.3; rigid rails)

$$F_{lat} = g_1(y_w, \psi_w) \tag{35}$$

$$M_{yaw} = g_2(y_w, \psi_w) \tag{36}$$

For each value of $y_w$ and $\psi_w$, the method determines the $F_{lat}$ which must be applied to obtain lateral equilibrium, and the $M_{yaw}$ needed for yaw equilibrium. By incrementing lateral excursion, while holding angle of attack constant, families of force-displacement and moment-displacement curves can be generated.

Figures 10 and 11 show examples of such curves for $\psi_w$ = -1.6° to $\psi_w$ = +1.6°. The wheel loads are $V_L = V_R$ = 12,500 lb, the coefficient of friction is $\mu$ = 0.3, no external drive torque is applied, and the rails are assumed to be rigid. The nominal creep coefficients used are half-Kalker values.* The test is performed using a new wheel on worn rail profile on standard gage, as shown in Figure 4, for the case of very mild curving (R = 10,000 ft).

The effects of creep force saturation and of vertical creep force components are exhibited in Figure 10. In the tread region of the profile ($y_w$ < 0.32 in), the magnitude of $F_{lat}$ saturates to $\mu$ x Axle Load (7500 lb) for large positive and negative angles of attack. On the flange ($y_w$ > 0.32 in), the vertical components of creep force help the left wheel climb the flange for positive angles of attack. This is due to the contributions of the lateral and spin creep which tend to lift the wheel off the rail. For negative angles of attack, the vertical creep forces, due to lateral creep, change direction and tend to press the wheel down harder against the rail, allowing the wheelset to support a much greater lateral force before derailment occurs.

Figure 11 shows the equilibrium wheelset yaw moment as a function of wheelset lateral excursion. For each angle of attack, $M_{yaw}$ is relatively small in the tread region and large in the flange region. As the wheelset contacts the flange, longitudinal creep forces saturate very quickly to the adhesion limit due to the sudden increase in rolling radius difference.

Maximum yaw moment in both the tread and flange regions occurs at zero angle of attack. As the angle of attack increases in either the positive or negative direction, $M_{yaw}$ decreases. This illustrates the coupling between the lateral and longitudinal creep forces. For a given level of creepage in a particular direction, the creep force in that direction is always a maximum when the creep forces in the other directions are zero.

The maximum lateral to vertical force ratio at the flanging wheel ($F_{YL}/V_L$ denoted as L/V) as a function of wheelset angle of attack is shown in Figure 12. This graph is indicative of the derailment tendencies of the wheelset. The peak L/V ratio increases significantly for negative $\psi_w$ until it saturates to Nadal's upper limit (16), given by

$$\left(\frac{L}{V}\right)_{upper} = \frac{\tan\delta_L + \mu}{1 - \mu\tan\delta_L} \tag{37}$$

where $(L/V)_{upper}$ is the largest value that the maximum lateral-to-vertical wheel force ratio can assume. Similarly, for large positive yaw angles, the maximum L/V ratio saturates to Nadal's lower limit,

$$\left(\frac{L}{V}\right)_{lower} = \frac{\tan\delta_L - \mu}{1 + \mu\tan\delta_L} \tag{38}$$

where $(L/V)_{lower}$ is the minimum value possible. For a flange contact angle of 64°, Nadal's limits predict: $(L/V)_{upper}$ = 6.11 and $(L/V)_{lower}$ = 1.08. These boundaries are marked in Figure 12. Garg and Weinstock (25) showed that the slope of the curve between Nadal's limits at intermediate yaw displacements is approximated by:

*Appropriate creep coefficients were used for the tread and the flange.

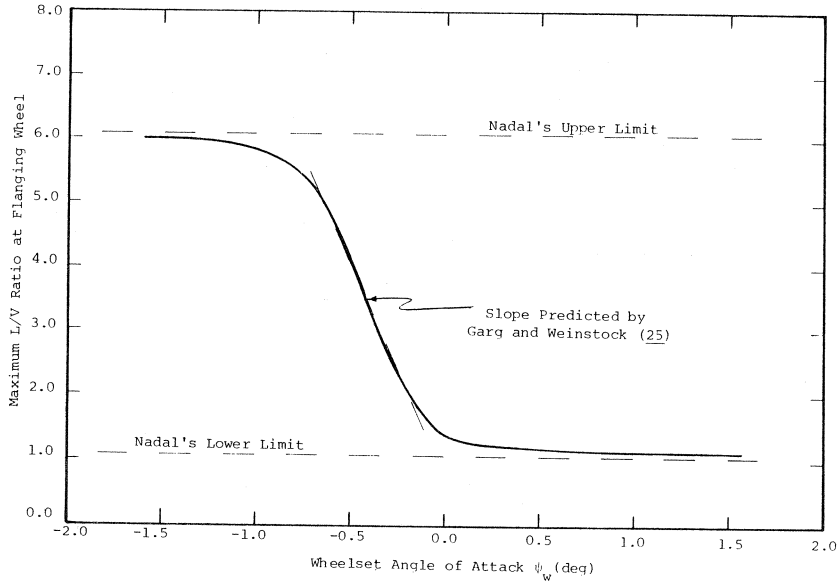


Fig. 12 Maximum L/V Ratio at Flanging Wheel vs Wheelset Angle of Attack (axle load = 25,000 lb; $\mu$ = 0.3; rigid rails)

This predicts a slope of -6.36/deg which agrees well with the slope obtained using our method.

To accommodate rail flexibility, the solution technique is to calculate the net lateral wheel force at each wheel assuming a rigid rail model. Then the lateral rail displacement at each wheel is calculated according to equations (10) and (11) and used to compute the effective lateral excursion at each wheel ($y_w - y_{rail_L}$, $y_w - y_{rail_R}$). These lateral excursions are used to update the wheel-rail contact geometry at the left and right contact points. The net lateral wheel force at each wheel is then computed, and the process is continued until convergence is achieved. Even with "soft" rail, convergence occurs rapidly, within several iterations.

The effect of including rail flexibility in steady-state curving studies is to increase the rail gage. This constant gage spread implies that the rails accommodate the large lateral wheel forces by moving out. The flexure of the rails results in greater lateral excursion of the wheelset by up to 30 or 40 percent, but the angle of attack of the wheelset is relatively unaffected. Also, the steady-state wheel-rail forces are not sensitive to flexure of the rail.

B. Two-Point Contact

For some profiles, two-point contact occurs at the outer (left) wheel when the net lateral excursion equals the flange clearance. To determine the wheel-rail forces and moments at the (three) contact patches, assuming rigid rails, four coupled equilibrium equations must be solved simultaneously: the spin, vertical, roll, and lateral equations. The lateral equation is then used to determine the equilibrium values of the contact forces and moments. This implies that the wheelset lateral force, derived from body and suspension forces, must be known. Once a solution to these coupled equations is determined, the wheelset yaw moment needed to satisfy yaw equilibrium is calculated from the yaw equation.

In a real vehicle, this yaw moment is provided by the suspension forces.

The four coupled equations are solved as before using two nested iteration loops as shown in Figure 13. The inner loop adjusts the spin perturbation rate, $\dot{\beta}$, to satisfy the spin equation. The outer loop adjusts the vertical components of the creep forces at the tread and the flange of the outer wheel and the tread of the inner wheel to simultaneously satisfy the lateral equation and the sum and difference of the vertical and roll equations. Once vertical force convergence is achieved, equilibrium values of all contact forces and moments are known and the yaw equation is used to calculate the wheelset yaw moment which must act for equilibrium.

Using this procedure, equilibrium values of wheelset yaw moment as functions of wheelset lateral force and angle of attack have been generated. The rails are assumed to be rigid and thus the wheelset lateral excursion is fixed at the flange clearance. Mathematically,

$$M_{yaw} = g_3(F_{lat}, \psi_w) \tag{40}$$

with $y_w = y_{fc}$ and $V_L$, $V_R$ known.

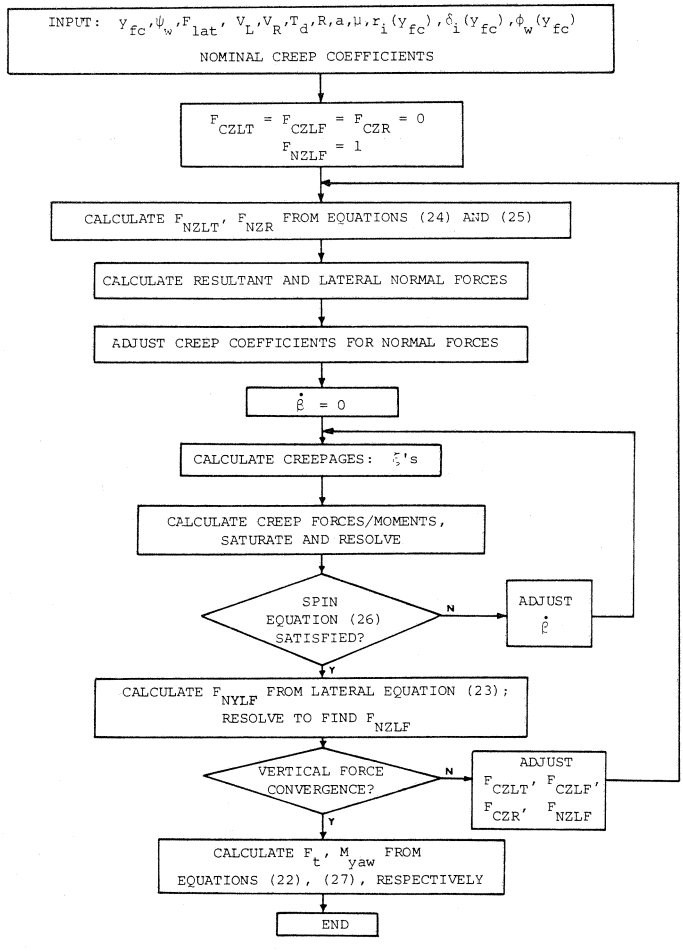


Fig. 13 Flowchart for wheelset equilibrium with rigid rails: two-point contact model

This function is plotted in Figure 14 for a wheelset with a fixed angle of attack of $\psi_w$ = +0.1° negotiating a 10° curve (i.e., R = 575 ft). Also shown in Figure 14 is the solution for a single-point contact analysis, obtained by cross-plotting equations (35) and (36).

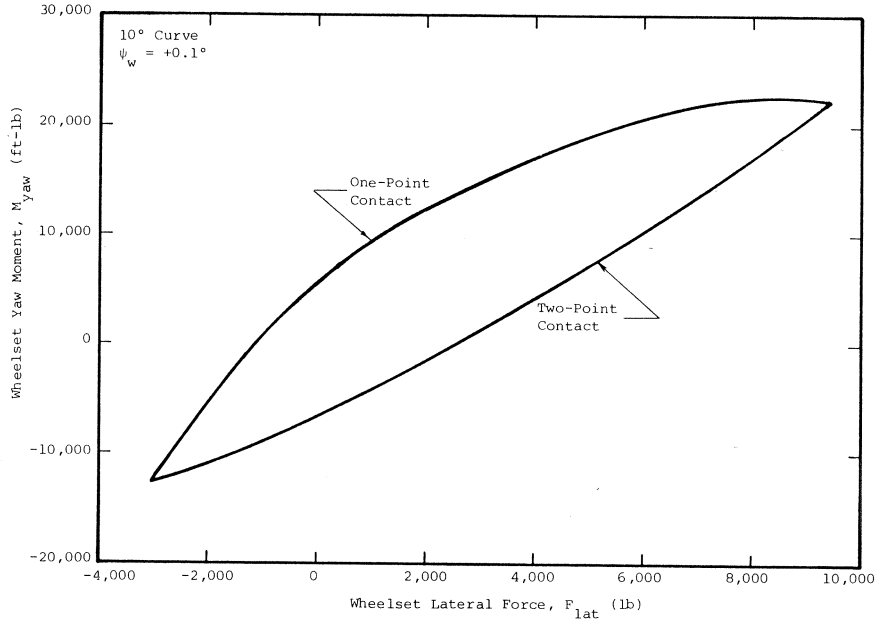


Fig. 14 Wheelset yaw moment vs. lateral force (10° curve; $\psi_w$ = +0.1°; rigid rails)

The equilibrium value of wheelset yaw moment predicted by the one-point contact analysis is larger than the moment calculated using the two-point analysis (for positive yaw moments). The yaw moment needed for equilibrium is equal and opposite to the yaw restoring moment provided by creep forces. The restoring moment helps to align the wheelset radially. Thus, the larger the restoring moment aiding to achieve radial alignment, the smaller the external forces required for equilibrium. These external forces are due to suspension forces which restrain the wheelset in a truck. Thus, since the one-point contact analysis predicts a larger equilibrium yaw moment, it suggests that the suspension forces needed for equilibrium will be lower than those predicted using the two-point contact analysis. Furthermore, the difference in yaw moments for the two analyses diminish with increased angles of attack.

The two-point analysis predicts large longitudinal creep forces in opposite directions in the tread and flange contact points of the flanging wheel. These opposing creep forces partially cancel one another. The one-point analysis predicts a longitudinal creep force at the flanging wheel which is larger than the net longitudinal creep force predicted using the two-point contact analysis. This larger longitudinal creep force results in the larger restoring moment.

The two-point analysis predicts lateral forces in opposite directions in the tread and flange contact points of the outer wheel as well. These lateral forces are the sum of the lateral components of the creep and normal forces at each contact point. The fact that the two-point analysis predicts large opposing contact forces at the flanging wheel is partly responsible for the significantly higher levels of total work expended as compared to the one-point analysis. (The total work is defined as in Equation (32)). Figure 15 compares the work at the flanging wheel computed using the one and two-point analyses as a function of wheelset lateral force. The results of the two-point analysis show that for large negative values of lateral force all the work is

expended at the tread contact patch and none at the flange contact patch. As the wheelset is loaded with more (positive) lateral force the flange contact patch work exceeds the work at the tread patch. The significant levels of work expended at the flange contact patch are attributed to large lateral and spin creepages (due to the large contact angle) and large creep forces which develop. Loading the wheelset with additional lateral force results in still higher levels of flange contact patch work, whereas the work at the tread diminishes as the force distribution shifts to the flange and away from the tread. This will continue until all the forces, and the work, vanish at the tread, and single-point flange contact is achieved. Figure 15 demonstrates the marked differences in contact patch work predicted using the two models.

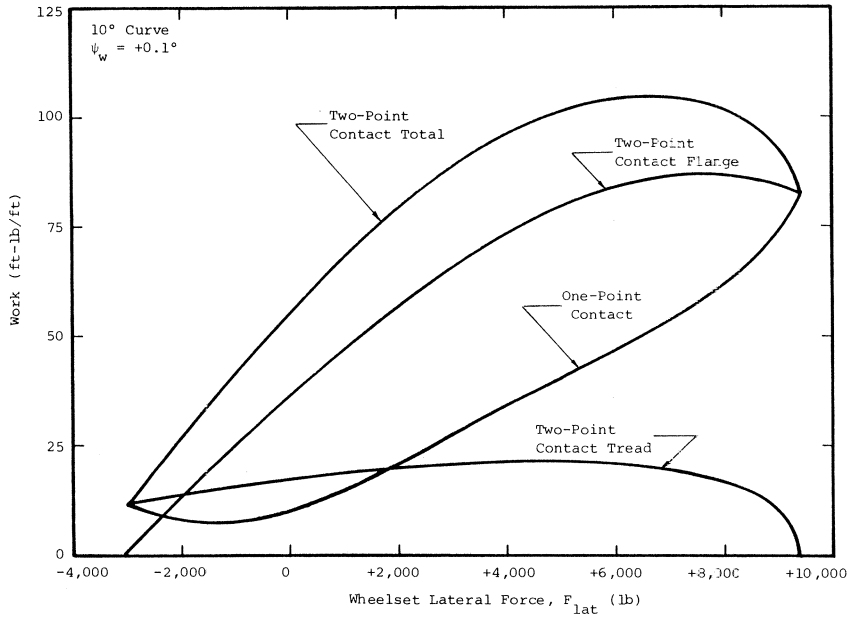


Fig. 15 Work at left wheel vs. wheelset lateral force (10° curve; $\psi_w$ = +0.1°; rigid rails)

Rail flexibility is accounted for, as before, by solving first for the net lateral wheel forces assuming rigid rails. Equations (10) and (11) are used to calculate the lateral rail displacements, where $F_{YL} = F_{YLT} + F_{YLT}$ in equation (10). The net lateral excursion at the right, $y_w - y_{railR}$, is computed and used to update the right contact geometry. It is assumed that two-point contact at the left wheel is maintained and thus $y_w - y_{rail_L} = y_{fc}$. The net lateral wheel forces are then computed and the procedure is continued until convergence occurs. As noted before, for typical values of lateral rail stiffness the rail gage and the wheelset lateral excursion are increased, but the wheelset angle of attack and wheel-rail forces are not significantly altered.

In the implementation of these wheelset models to more complete analyses of vehicle steady-state curving the lateral force and yaw moment needed for wheelset equilibrium are provided by suspension and body forces. The single-point and/or two-point contact models are then incorporated as subroutines in a larger vehicle program. Reference (12) illustrates this procedure for single-point contact, while (26) discusses the full vehicle model using two-point contact.

## CONCLUSIONS

This paper has shown the equation formulation and numerical solution method necessary to compute the forces, moments, and geometry of a wheelset during

steady-state curve negotiation. The formulation includes both single-point and two-point wheel-rail contact. The wheelset models presented are the most important elements in any total vehicle model and thus merit such a detailed discussion.

Typical numerical results for both the single and two-point contact models were presented and a comparison of their force/moment and related wear index characteristics was given. It was shown that in general the single-point model overpredicts the steering capability of the wheelset and underpredicts the amount of work (wear) done on the flanging wheel.

ACKNOWLEDGEMENTS

The authors acknowledge the technical contributions of Dr. H. Weinstock of the U.S. Department of Transportation (Transportation Systems Center) and of Mr. J. Elkins of The Analytic Sciences Corporation with respect to the two-point contact problem. Support for the work described in this paper was provided in part by the Association of American Railroads (Chicago Technical Center) and by the U.S. D.O.T. (UMTA).

REFERENCES

1. Eksergian, R., "Static Adjustments of Trucks on Curves," ASME Transactions, Vol. 42, No. 1776, 1921.

2. Porter, S.R.M., "The Mechanics of a Locomotive on Curved Track," The Railway Gazette, 1935.

3. Vermeulen, P.J. and Johnson, K.L., "Contact of Nonspherical Elastic Bodies Transmitting Tangential Forces," J. of Applied Mechanics, Vol. 86, June 1964, pp. 338-340.

4. Kalker, J.J., "Survey of Wheel-Rail Rolling Contact Theory," Vehicle System Dynamics, Vol. 5, 1979, pp. 317-358.

5. Newland, D.E., "Steering a Flexible Railway Truck on Curved Track," J. of Engineering for Industry, A.S.M.E. Transactions, Series B, Vol. 91, No. 3, August 1969, pp. 908-918.

6. Boocock, D., "Steady-State Motion of Railway Vehicles on Curved Tracks," J. of Mechanical Engineering Science, Vol. 11, No. 6, December 1969, pp. 556-566.

7. Bell, C.E., Horak, D., and Hedrick, J.K., "Stability and Curving Mechanics of Rail Vehicles," J. of Dynamic Systems, Measurement, and Control, Vol. 103, September 1981, pp. 181-190.

8. Horak, D., Bell, C.E., and Hedrick, J.K., "A Comparison of the Stability and Curving Performance of Radial and Conventional Rail Vehicle Trucks," J. of Dynamic Systems, Measurement and Control, Vol. 103, September 1981, pp. 191-200.

9. Elkins, J.A. and Gostling, R.J., "A General Quasi-Static Curving Theory for Railway Vehicles," Proc. 5th VSD-2nd IUTAM Symposium on the Dynamics of Vehicles on Roads and Tracks, 1978.

10. Law, E.H. and Cooperrider, N.K., "Nonlinear Dynamic and Steady-State Curving of Rail Vehicles," presented at the 1978 A.S.M.E. Winter Annual Meeting, San Francisco, CA, December 1978.

11. Hedrick, J.K., Wormley, D.N., Arslan, A.V., and Chin, R., Nonlinear Analysis and Design Tools for Rail Vehicles: Nonlinear Locomotive Dynamics, A.A.R. Report R-463, December 1980.

12. Bell, C.E., Curving Mechanics of Rail Vehicles, Ph.D Thesis, Department of Mechanical Engineering, M.I.T., September 1981.

13. Bell, C.E., and Hedrick, J.K., "Forced Steering of Rail Vehicles: Stability and Curving Mechanics," Vehicle System Dynamics, Vol. 10, pp. 357-386, 1981.

14. Marcotte, P., Mathewson, K.J.R., and Young, R., "A Practical Model of Rail Vehicle Curve Negotiation," Presented at the 7th Symposium of the IAVSD, Cambridge, UK, September 1981.

15. Sweet, L.M. and Sivak, J.A., "Nonlinear Wheelset Forces in Flange Contact, Part 1: Steady State Analysis and Numerical Results," J. of Dynamic Systems, Measurement and Control, Vol. 101, No. 3, September 1979, pp. 238-246.

16. Gilchrist, A.O. and Brickle, B.V., "A Re-Examination of the Proneness to Derailment of a Railway Wheelset," J. of Mechanical Engineering Science, Vol. 18, No. 3, 1976, pp. 131-141.

17. Doyle, G.R., "Conventional Versus Self-Steering Radial Trucks for High-Speed Passenger Trains," ASME Report 79-RT-3, ASME/IEEE Joint Railroad Conference, 1979.

18. Elkins, J.A. and Eickhoff, B.M., "Advances in Non-Linear Wheel/Rail Force Prediction Methods and Their Validation," presented at the ASME Winter Conference, New York, December 1979.

19. Bolton, P., "Wear of BS11 Rail Steels in Rolling/Sliding Contact with Class "D" Type Steel," British Railways Technical Note TNMET21, February 1980.

20. Kalkstein, J.L. and Zaremba, L.A., "Safety Life Cycle Methods for Evaluating Railway Wheelsets," The Aerospace Corporation, 1981.

21. Kumar, S., Prasanna Rao, D.L., and Rajkuma, B.R., "A Wheel-Rail Wear Study for Railroad Transit Systems," I.I.T. Report IIT-TRANS-80-1, August 1980.

22. Bolton, P.J., Clayton, P. and McEwen, I.J., "Wear of Rail and Tyre Steels Under Rolling/Sliding Conditions," British Rail Research, presented at the ASME/ASNE Conference, August 1980.

23. Cooperrider, N.K. and Law, E.H., Data Book: Wheel/Rail Geometry for Five Wheel Profiles and Three Rail Profiles, Report No. ERC-R-75015, Department of Mechanical Engineering, Arizona State University, Tempe, Arizona, 85281.

24. Ahbeck, D.R., "The Effects of Track Modulus on Vehicle-Track Dynamic Interaction," IEEE/ASME Railroad Conference, Erie, PA, 1982.

25. Garg, D. and Weinstock, H., "Piecewise Linear Approximation of Lateral Forces in Rail-Wheel Contact," Transportation Systems Center, U.S. Department of Transportation, August 1980.

26. Wormley, D.N., Hedrick, J.K., Nagurka, M.L., Surjana, J., "Performance Limits for Urban Rail Transit Trucks - Interim Report," Transportation Systems Center, June 1982.

APPENDIX A - CREEP FORCE MODEL

The "heuristic" nonlinear creep force model mentioned in the text is a modified Vermeulen-Johnson (3) formulation that includes the effect of spin creep.

The creep forces and moments are initially computed using the Kalker linear theory (4). At each contact patch, the longitudinal and lateral components of creep force are:

$$F'_{CPX} = -f_{33}\xi_x \qquad (A\text{-}1)$$

$$F'_{CPY} = -f_{11}\xi_y - f_{12}\xi_{SP}$$

and the spin creep moment acting normal to the contact patch is:

$$M_{CP} = f_{12}\xi_y - f_{22}\xi_{sp} \qquad (A\text{-}2)$$

where $\xi_x$, $\xi_y$ and $\xi_{sp}$ are the longitudinal, lateral, and spin creepages*, respectively, in contact patch coordinates. The derivation of these creepages is a complicated application of kinematics (18,26). The creepages at the left and right contact patches are:

$$\xi_{x_L} = 1 + \frac{a}{R} - r_L\rho \tag{A-3}$$

$$\xi_{x_R} = 1 - \frac{a}{R} - r_R\rho \tag{A-4}$$

$$\xi_{y_L} = -r_L\rho\ \psi_w \sec(\delta_L + \phi_w) \tag{A-5}$$

$$\xi_{y_R} = -r_R\rho\ \psi_w \sec(\delta_R - \phi_w) \tag{A-6}$$

$$\xi_{SP_L} = -\rho\sin(\delta_L + \phi_w) - \frac{1}{R}\cos(\delta_L + \phi_w) \tag{A-7}$$

$$\xi_{SP_R} = \rho\sin(\delta_R - \phi_w) - \frac{1}{R}\cos(\delta_R - \phi_w) \tag{A-8}$$

where $\rho \triangleq \frac{\Omega}{V} = \frac{1}{r_o} + \frac{\dot{\beta}}{V}$. (For the case of two-point contact at the left wheel, equations (A-3), (A-5), and (A-7) are the creepages at the left tread and left flange contact patches when the appropriate rolling radii and contact angles are used). The derivations of equations (A-3) - (A-8) make use of the expression for the shift of the contact patch due to $\psi_w$. The longitudinal shift of the contact patch is given by (16).

$$\Delta_{x_i} = r_i\psi_w\tan(\delta_i \pm \phi_w) \tag{A-9}$$

The creep coefficients $f_{11}$, $f_{12}$, $f_{22}$, and $f_{33}$ are functions of the wheel-rail geometry, material properties, and resulting normal load. They are computed according to Kalker's linear theory (4). Typically these calculated values are reduced by 50% to account for discrepancies between field and laboratory test data due to contaminated rail conditions in the field.

The creep coefficients are functions of the normal load, N, calculated in the following way:

$$\begin{aligned} f_{11} &= \left(\frac{N}{N_N}\right)^{2/3} f_{11_N} \\ f_{12} &= \left(\frac{N}{N_N}\right) f_{12_N} \\ f_{22} &= \left(\frac{N}{N_N}\right)^{4/3} f_{22_N} \\ f_{33} &= \left(\frac{N}{N_N}\right)^{2/3} f_{33_N} \end{aligned} \tag{A-10}$$

where $f_{ij_N}$ are the nominal values computed for the nominal normal load $N_N$ and $f_{ij}$ are the values for normal load, N.

The magnitude of the resultant creep force cannot exceed the amount of available adhesion, $\mu N$, at the wheel-rail contact interface. The creep force saturation is computed according to a modified Vermeulen-Johnson model in which a saturation coefficient is determined by:

*The creepages are the relative velocities between the wheel and rail at the contact patch normalized by the nominal forward velocity.

$$\varepsilon = \begin{cases} \frac{\mu N}{F'_R}\left[\left(\frac{F'_R}{\mu N}\right) - \frac{1}{3}\left(\frac{F'_R}{\mu N}\right)^2 + \frac{1}{27}\left(\frac{F'_R}{\mu N}\right)^3\right] & \text{for } F'_R < 3\mu N \\ \frac{\mu N}{F'_R} & \text{for } F'_R > 3\mu N \end{cases} \tag{A-11}$$

where the unlimited resultant creep force is:

$$F'_R = +\sqrt{(F'_{CPX})^2 + (F'_{CPY})^2} \tag{A-12}$$

The saturated creep forces are then given by:

$$\begin{aligned} F_{CPX} &= \varepsilon F'_{CPX} \\ F_{CPY} &= \varepsilon F'_{CPY} \end{aligned} \tag{A-13}$$

# Computational Methods in Ground Transportation Vehicles

*presented at*

THE WINTER ANNUAL MEETING OF
THE AMERICAN SOCIETY OF MECHANICAL ENGINEERS
PHOENIX, ARIZONA
NOVEMBER 14-19, 1982

*sponsored by*

THE APPLIED MECHANICS DIVISION, ASME
THE DYNAMIC SYSTEMS AND CONTROL DIVISION, ASME

*edited by*

M. M. KAMAL
GENERAL MOTORS RESEARCH LABORATORIES

J. A. WOLF, JR.
GENERAL MOTORS RESEARCH LABORATORIES

THE AMERICAN SOCIETY OF MECHANICAL ENGINEERS
United Engineering Center 345 East 47th Street New York, N. Y. 10017

Library of Congress Catalog Card Number 82-73171